Volume 19, Issue 2, 192524 (1-9)

Majlesi Journal of Electrical Engineering (MJEE)

https://doi.org/10.57647/j.mjee.2025.1902.24

Detection of oil slicks in SAR satellite images using Otsu-Bradley's thresholding method

Farzane Mahdikhani, Mohammadreza Hassannejad Bibalan*

Department of Electrical Engineering, Imam Khomeini International University, Qazvin, Iran.

*Corresponding author: mhbibalan@ikiu.ac.ir

Original Research

Received:
12 March 2025
Revised:
7 April 2025
Accepted:
30 April 2025
Published online:
1 June 2025

Abstract:

This paper proposes a novel thresholding method for oil slick detection from synthetic aperture radar (SAR) images using modified Otsu and Bradley's approaches. The existence of oil sources in the seas causes hydrocarbon stains to appear on the surface of the seas and as a result, it leads to a decrease in the quality of these waters. Oil slicks are distinguished from the sea surface through the utilization of a combined Otsu-Bradley's quantization technique, logical operators, and averaging the input image, while categorizing the classes based on the geometrical, textural, and radiometric properties of the images. We aim to enhance the identification of oil spills by utilizing remote sensing techniques, SAR satellite imagery processing, thresholding methods, and extracting geometric and textural features. We performed the classification process several times, and KNN classification method revealed an accuracy of 94.9%. Furthermore, KNN achieved a precision of 92.4%, so we repeated the classification using two selected features, area and entropy to reach a precision of 96.36%.

Keywords: Oil slick detection; SAR satellite images; Texture features; Geometric features; Otsu-Bradley thresholding

Nomenclature

Convolutional blind denoising network	CBD-Net
Convolutional neural network	CNN
K-nearest neighbors	KNN
Mean squared error	MSE
Orientation-shared convolutional network	OSC-Net
Peak signal to noise ratio	PSNR
Radial basis function support vector machine	RBF-SVM
Synthetic aperture radar	SAR
Structural similarity index	SSIM

1. Introduction

With the rapid growth of the economy in the world, the extraction of oil resources and maritime transportation have intensified, and in proportion to this progress, the amount of unwanted oil spills into the sea has increased. Therefore, to reduce environmental risks, it is necessary to consider a suitable way to identify the contaminated area and the amount of contamination with the leaked oil substance. Obtaining this information from the contaminated area is very important for countermeasures to remove the contamination [1].

When an oil spill occurs, the location and extent of the oil spill must be determined. With timely knowledge of the location of the oil spill and the direction of its movement, planned actions can be taken to reduce its effects on the environment. In this regard, remote sensing data play a very important role by providing information about the amount and direction of oil slick movement in predicting the movement of oil slicks as well as supporting oil slick control and cleanup operation [2].

One of the important sources of pollution are oil rigs, especially when an accident occurs in them, it causes a lot of environmental and economic damage. The harmful effects of marine pollution are numerous, in addition to economic losses, it leads to global climate change and damage to aquatic ecosystems. Considering that the sea is a valuable platform for oil reserves and the place of oil extraction and the traffic of carrier ships, it is necessary to quickly identify oil spots in order to prevent oil spills and reduce its destructive effects on marine ecosystems. The large size of the water areas has made continuous monitoring of oil spills on them by conventional methods such as on-site ship visits expensive, time-consuming and practically difficult.

Recent advances in remote sensing technology have made it a suitable alternative to traditional oil spill detection and analysis methods. Wide coverage of areas, high time frequency, digital data structure, types of sensors with high variety of information are among the reasons for using remote sensing in oil spill monitoring. SAR sensors are highly sought after for their ability to capture images at any time of the day or night, perform in any weather conditions, and capture high-resolution images of large areas. However, the presence of speckle noise in SAR images makes their segmentation process difficult [3]. When oil spreads on the sea surface, it causes the capillary waves of the sea to be damped and the sea surface to be smooth, and the received reflected waves are reduced, and less energy reaches the sensor. In this case, these areas are seen as dark spots in radar images [4]. These reflected sea surface waves have constructive and destructive interference that appears as speckle noise in SAR images [5].

In addition to oil slicks, low wind areas or convective cells or rain cells are also seen in dark form in radar images [6]. Oil spill detection includes three main steps: dark spot extraction, feature selection, and classification. The detection of dark regions is a long step, and the overall accuracy strongly depends on this step and has a great influence on the accuracy of the next two steps. Since the ability to detect oil spills and the like is an important point, in the next step, a suitable feature vector must be selected to separate areas contaminated by oil spills and the like to be used as the input vector of the classification stage [7].

Traditional segmentation methods use texture and geometric features to segment images regionally. Recent studies have focused on oil slick detection using deep neural networks. The article [8] introduces the convolutional blind denoising network (CBD-Net), an end-to-end convolutional neural network designed for detecting oil fields on surface SAR images. The CBD-Net utilizes multi-purpose features to accurately segment fine-grained oil spills, even in cases where the target class is not clearly distinguishable from the background in SAR images. Experimental results demonstrate that CBD-Net outperforms other models in extracting oil spill areas from complex images, particularly in dark spots and complex scenes. In another study [9], the orientation-shared convolutional network (OSCNet), a neural convolutional neural network, is used to detect oil spills in SAR images which consists of 16-VG layers and it has been trained on a dataset of dark areas. The OSCNet shows improved performance compared to methods using manual features, showcasing its ability for oil slick detection.

A two-stage point convolutional neural network for detecting ships and oil slicks in SLAR images is presented in article [10]. The architecture includes three pairs of convolutional neural networks (CNNs) trained to recognize ships, oil, and beaches. After classification, a morphological expansion filter is applied to remove small dark areas.

Clustering algorithms, logistic regression, and convolutional neural networks are combined in [11] to detect marine oil spills. A cross neural network is integrated into a decision support system to speed up analysis and diagnosis. Additionally, a two-stage deep environment for detecting oil occurrences is introduced in article [12], which involves classifying dark spots based on oil spill percentages and using U-Net to accurately identify and classify oil slicks. Recently [13] presents a method for detecting oil spills in PolSAR images using deep multi-layer features with CNN. The PolSAR data is converted into a 9-channel block for input into the CNN, which automatically extracts high-level features. These features are further reduced using principal component analysis (PCA) and fed into a radial basis function support vector machine (RBF-SVM) for classification. Three fully polarized SAR datasets are used for training and evaluation.

Our proposed method incorporates the advantages of Otsu's and Bradley's thresholding techniques with additional features. Otsu's method maximizes the between-class variance of pixel intensities to find an optimal threshold for separating oil spill pixels from the background. We apply Otsu's thresholding to the SAR images to identify potential oil spill regions. Bradley's method adapts the threshold locally based on a pixel's neighborhood, addressing uneven illumination and varying oil slick sizes. We use Bradley's thresholding to refine the initial oil spill detection.

Furthermore, the geometrical features (such as area, perimeter, and compactness) and textural features (such as entropy and contrast) have been extracted from the detected oil spill regions. These features provide additional discriminative information for accurate segmentation.

The rest of the paper is organized as follows. The problem has been stated in section 2. The proposed method which includes dark spot detection based on Otsu-Bradley's thresholding is presented in section 3. Evaluation, dataset and simulation results include the feature extraction, classification, and experimental results, are given in sections 4 and 5. The paper is concluded in section 6.

2. Oil slicks detection problem in SAR satellite images

Oil spills result from accidents involving oil tankers, pipelines, and other sources. These spills can harm marine ecosystems, aquatic organisms, and bird species. SAR sensors, deployed on satellites or planes, capture reflected radio waves from various surfaces, including ships, sea, land, and oil spills. However, distinguishing between oil slicks and look-alikes (such as grease ice or sea waves) in SAR images remains challenging due to their similar dark dot appearance. For image segmentation, thresholding can be used as an effective tool to separate the object from the background when the gray levels between them are significantly different. In general, in image thresholding, a threshold value is specified for the pixels of the image, and this threshold level can be a global threshold level for all pixels, or a separate threshold level for each pixel. Thresholding is used as a method to select the desired areas of the image, and remove the areas that are not important.

2.1 Otsu's method

Consider that the pixels in a given image be indicated in L gray levels (1,2,...,L). Let n_i explain the number of pixels at level i, and N explain the general number of pixels $N = \sum_{i=1}^{l} n_i$, the probability of occurrence of level i is given by $p_i = n_i/N$. Let an image with threshold T be divided into two classes C_0 and C_1. C_0 contains of pixels with levels [1,...,T] and C_1 contains of pixels with levels [$T+1$,...,L]. ω_1 and ω_2 explain the cumulative probabilities, μ_0 and μ_1 explain the mean levels, respectively. These amounts are given by [14],

$$\omega_1 = \sum_{i=1}^{t} p_i \tag{1}$$

$$\omega_2 = \sum_{i=t+1}^{L} p_i \tag{2}$$

$$\mu_1 = \frac{\sum_{i=1}^{t} ip_i}{\omega_1} \tag{3}$$

$$\mu_2 = \frac{\sum_{i=t+1}^{L} ip_i}{\omega_2} \tag{4}$$

μ_T, σ_b^2 explain the mean level of the image and the between-class variance, respectively,

$$\mu_T = \sum_{i=1}^{L} iP_i \tag{5}$$

$$\sigma_b^2 = \omega_1(\mu_1 - \mu T)^2 + \omega_2(\mu_2 - \mu T)^2 \tag{6}$$

The threshold provided by Otsu's method for binary images is the maximum between-class variance [8],

$$T = \arg\max\{\sigma_b^2(T)\}, \quad 1 \le T \le L \tag{7}$$

Otsu's thresholding works well when the pixels of the image generally consist of two brightness groups, in other words, this method works well when the histogram of the image contains two peaks. When the background of the input image is not uniform, choosing a global threshold limit it will not be possible for all pixels of the image, because in this case, the selected threshold limit may be suitable for one area of the image and not for another.
As a result, not all image pixels are correctly converted to binary. Increasing the pixel intensity difference between the dark areas of the image and the bright areas of the image improves the thresholding performance of Otsu's. For this purpose, the intensity of each pixel of the input image is multiplied by 2, then it is considered as input data. Fig. 1 shows an example in this case.

2.2 Bradley's method

Bradley's method takes help from neighboring pixels in all directions to determine the threshold limit of each pixel [9]. In such a way that initially a number of neighboring pixels in a selection window and then the average value of the brightness intensity of the neighboring pixels is calculated, which is used as the threshold limit of the desired pixel. The average calculation is done using the integral image.
Calculating the sum of pixel values in an image using integral image is a quick and efficient method. In most instances in image processing, the image integral is utilized to determine the average brightness of the image.
The image integral leads to a significant decrease in the amount of computational operations, resulting in a substantial reduction in execution time. The sum of a pixel and its adjacent pixels above and to the left equals the integral of the desired pixel in the image. Then the comparison operation is performed. According to the fact that the desired pixel is T percent lower than the average of the neighboring, pixels to black, otherwise the face turns white. To calculate the average of the desired pixel in the neighborhood (3×3) from the integral image, the highlighted neighboring pixels

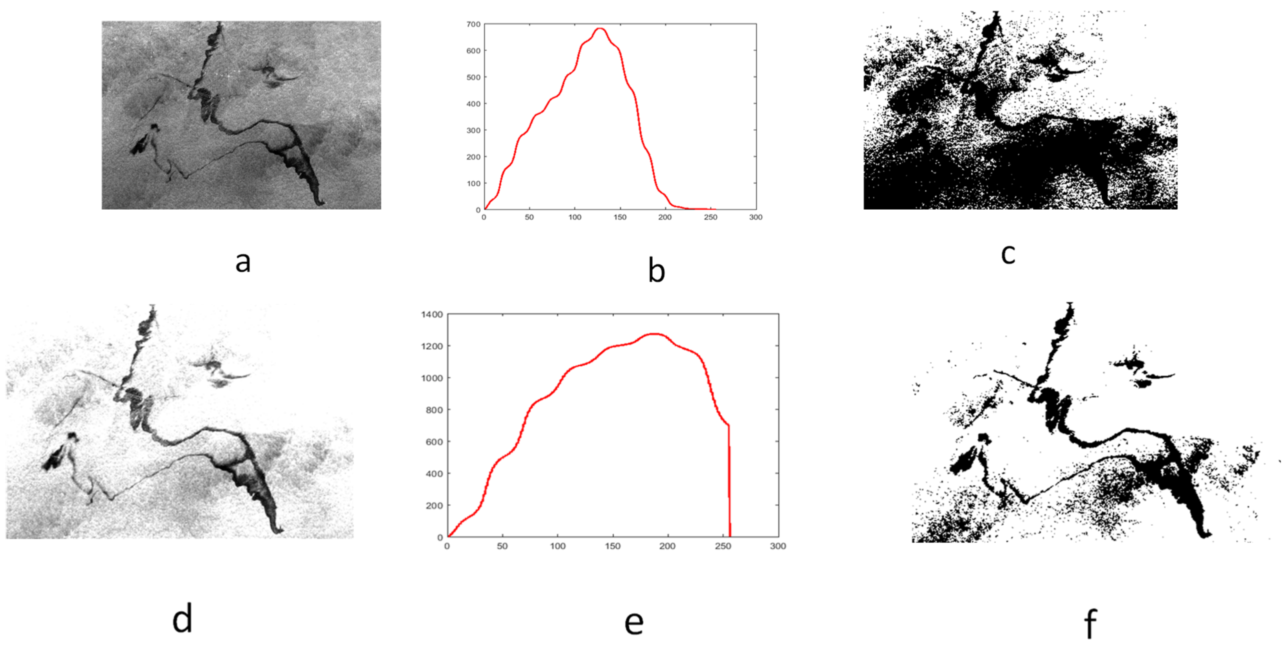

Figure 1. (a) Input image, (b) histogram, (c) Otsu's thresholding, (d) input enhancement, (e) enhanced histogram, (f) Otsu's thresholding.

are used [15].

$$M = \frac{1}{9}\{[(x+1,y+1)-(x-2,y+1)]-[(x+1,y-2)-(x-2,y-2)]\} \tag{8}$$

$$p(n) = \begin{cases} 1, & p(n) > M\left(\frac{100-T}{100}\right) \\ 0, & p(n) < M\left(\frac{100-T}{100}\right) \end{cases} \tag{9}$$

where $p(n)$ is the brightness of the nth pixel, T is the selected percentage value and M is the average pixel (x,y) of the selected neighbors, according to the below matrix. Choosing the right T value in Bradley's thresholding is crucial as it significantly affects the outcome of the thresholding process. In this study, we evaluated the range of $15 < T < 30$. For each T value, we computed the PSNR of the oil data thresholded output images and the image mask using specific criteria. The Bradley method showed the most effective scaling performance, with the highest PSNR achieved at $T = 23$.

$x-2,y-2$	$x-2,y-1$	$x-2,y$	$x-2,y+1$	$x-2,y+2$
$x-1,y-2$	$x-1,y-1$	$x-1,y$	$x-1,y+1$	$x-1,y+2$
$x,y-2$	$x,y-1$	x,y	$x,y+1$	$x,y+2$
$x+1,y-2$	$x+1,y-1$	$x+1,y$	$x+1,y+1$	$x+1,y+2$
$x+2,y-2$	$x+2,y-1$	$x+2,y$	$x+2,y+1$	$x+2,y+2$

3. Proposed Otsu-Bradley's thresholding

A binary image consists of pixels of ones and zeros. These one and zero pixels can be imagined as false and true. By clarifying this concept, we can apply logical operations on binary images. Logical operations compare two input pixels from two binary images with the same size and then produce an output image with the same size as output. In addition, we can develop logical operations to process black and white images. Table 1 shows the correctness of the logical operator on the data.

Table 1. The logical operator OR and AND [16].

A	B	A&&B	A||B
False	False	False	False
False	True	False	True
True	False	False	True
True	True	True	True

We can imagine the performance of Otsu's and Bradley's thresholding methods on oil slick images in three ways. Images that Otsu's method can threshold well, images that Bradley's method performed better, or images that both methods provided acceptable performance.

According to the simulations on the SAR oil slick data, the images in which the oil slick is spread and not in the form of a line, and a large area of the image is made up of dark pixels of the oil slick, the performance of Otsu's method is better, because in this case, the contrast of the image between the oil slick and the sea surface increases, but Bradley's method does not perform well because this method is measured relative to the neighboring pixels, and many interior points of the oil slick are not detected. In this case, it is better to select all pixels detected by both methods as oil slick pixels.

In this type of images, because the number of dark oil pixels is large, the average of the whole image is low, and the pixel selected by the Otsu's method for thresholding, because it is calculated according to the probability of each class, is less than the average of the whole image. In the images where the oil slick is in the form of a line and part of the background of the image is dark, Otsu's method is not able to threshold, because the dark part of the image is also identified as an oil slick, but Bradley's method is able to threshold better. In this case, it is better to select the common points identified in both methods as oil slick pixels. For images where the oil slick is linear and the image background is bright, both methods provide acceptable performance. The proposed flowchart, which is a combination of two thresholding methods, Otsu and Bradley, is shown in Fig. 2 where,

M = mean of the input image

A = Image thresholded by Otsu's method

B = Image thresholded by Bradley's method ($T = 23$)

C = A − B

D = pixels obtained by Otsu's method for thresholding.

The proposed flowchart is created by examining the geometric and textural aspects of the input images, and is developed by consolidating the outcomes of algorithmic tests based on the flowchart. In this research, the goal is to attain maximum accuracy by following a suggested flowchart to minimize speckle noise. A 5×5 median filter is applied, and the filtered information is quantified using Otsu and Bradley techniques. We also compute the mean of the input image and the pixel chosen as the threshold using the Otsu technique. If the mean of the input image was lower than the pixel value, we combine the thresholded output images of Otsu and Bradley using the logical operator "OR", while the results are combined using the logical operator "AND" if it was higher. There are only a small number of images where both techniques can detect oil stains completely, with each technique only detecting a portion of the oil stains. To fully identify objects in these images, we apply the Bradley Otsu and "OR" image outputs and take the difference between them.

4. Assessment criterions

The main types of slicks that often appear in SAR images are reported in the following [17]:

Natural biogenic slicks: These are surface films formed by volume scattering decay in a rain system, also creating a low

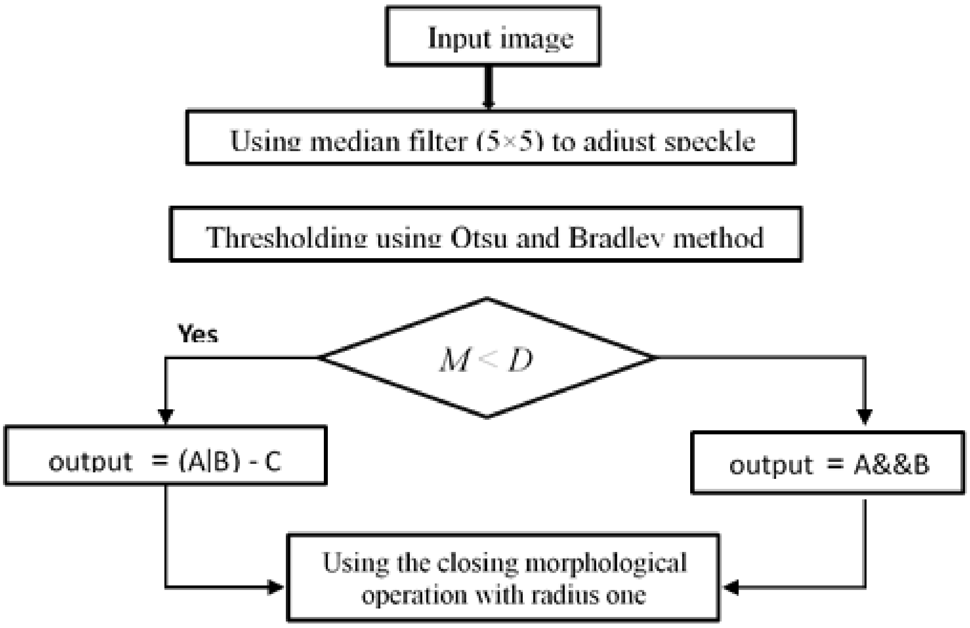

Figure 2. Proposed flowchart of the proposed Otsu-Bradley's thresholding.

backscattering region. This is problematic in higher marine organisms. This category is the most complex oil spill to look like, as the radar signatures of biogenic spills can be quite similar to mineral oil films. Since the only oil spills considered in this paper are anthropogenic spills, naturally occurring biogenic spills are grouped as similarity.

Low wind zones: The roughness of the sea surface depends on the wind speed and the change in the wind speed changes the capillary waves of the sea. Low wind speed (wind speed less than 3 m/s) creates a low backscatter region. Which causes dark spots similar to oil slicks.

Rain effects: Rain cells dampen capillary waves when they hit the sea surface. As a result, spots similar to oil slicks appear in the radar images in rainy areas.

Sea ice: Sea ice is defined as frozen ocean water that can be growing or melting. So the SAR scatter of sea ice depends primarily on the type of ice and therefore can be quite diverse due to the wide range of ice types. Sea ice texture in SAR images is relatively complex. They can be roughly characterized by blurred shapes, three-dimensional structure, sharp fractures and high contrast (dark and bright points).

Micro convective cells: The local temperature difference between the air and the sea causes intense vertical exchange of heat. The upper/lower air creates a cell shape that results in a horizontal change in sea surface wind speed. This wind variability modulates the centimeter-scale waves and thus the capillary waves of the sea. Therefore, cellular patterns are usually visible in SAR images.

To evaluate the function of the proposed algorithm, three common metrics including PSNR, SSIM, and MSE are used for all thresholding results. These three criteria are defined as follow [18].

Peak Signal to Noise Ratio (PSNR):

PSNR calculates the maximum signal-to-noise ratio in decibels, between two images. This ratio is used as a quality measure between the image thresholded and the image mask.

$$=10\log_{10}\frac{255^2}{\text{MSE}} \tag{10}$$

Mean Squared Error (MSE):

MSE is a metric for assessing the quality and discrepancy between the original image and a distorted (reconstructed or compressed) image.

$$\text{MSE} = \frac{1}{MN}\sum_{i=0}^{m-1}\sum_{j=0}^{n-1}(f(i,j)-h(i,j))^2 \tag{11}$$

where M and N represent the number of rows and columns in the image matrix respectively. $f(i,j)$ and $h(i,j)$ represent the gray level of the original image and the image thresholded in the ith row and jth column respectively.

Structural Similarity Index (SSIM):

It calculates the similarity between the image thresholded and the image mask by measuring the three criteria of brightness, contrast and structural similarity.

$$\text{SSIM} = \left(\frac{2\mu_X\mu_Y+C_1}{\mu_X^2+\mu_y^2+C_1}\right)^{\alpha}\left(\frac{2\sigma_X\sigma_Y+C_2}{\sigma_X^2+\sigma_y^2+C_2}\right)^{\beta}\left(\frac{\sigma_{XY}+C_3}{\sigma_X\sigma_Y+C_3}\right)^{\gamma} \tag{12}$$

where μ_X and μ_Y represent the average intensity of the mask image and image thresholded respectively. σ_X and σ_Y are the standard deviation of the mask image and the image thresholded respectively. σ_{XY} represents the covariance between the mask image and the thresholded image. C_1, C_2 and C_3 are some constants and α, β, γ are weights which usually equal to 1.

To check the performance of the proposed algorithm, we evaluated the three criteria PSNR, MSE and SSIM on 206 oil slick data. Fig. 3 shows the results of this evaluation.

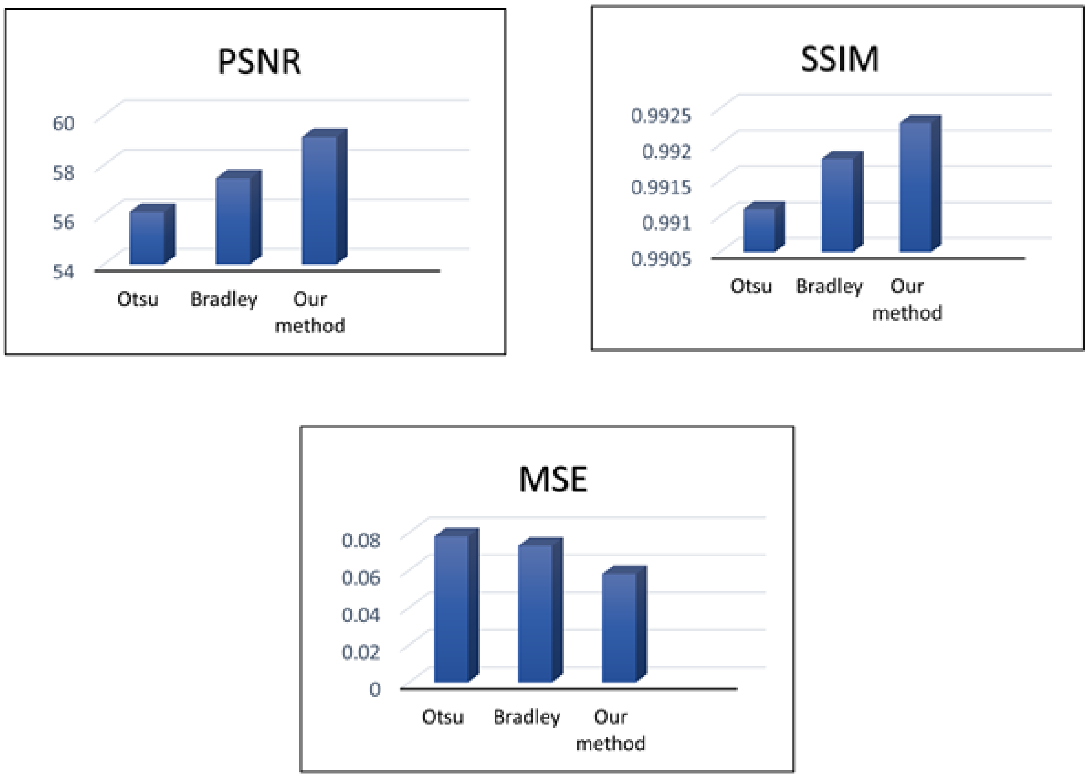

Figure 3. Quality assessment based on different criterions: PSNR (scalar), SSIM, MSE (normalized).

We used 300 dataset images, 206 oil spills and 94 look-alikes images with resolution 256×256 pixels. Based on the results from Fig. 3, the mentioned algorithm achieved higher PSNR and SSIM values compared to the two other methods, while demonstrating lower MSE. Additionally, the findings indicate that Otsu's enhanced technique outperforms Bradley's method in distinguishing the oil slick from the sea surface.
In Fig. 4, our algorithm successfully distinguished the oil data from the sea surface, each collected from different satellites with varying geometric and textural features.

4.1 Spot features selection

The features commonly used to detect oil slicks can be broadly classified into three main categories, characteristics related to the geometric features of oil slicks (e.g., perimeter, area), characteristics related to the physical behavior of oil slicks (e.g., mean, variance), and the characteristics of the reference to the oil slicks in the image (e.g., Distance from land and oil platform, etc.). The following features used are listed as [19]:
Entropy: The entropy property determines the uniformity of the intensity of the image pixels. Images that have uniform brightness, they have more entropy. The lowest entropy value is when all the pixels of the image have the same light intensity. The entropy of an image is defined (12) as follows:

$$H = -\sum_{i}\sum_{j} p(i,j) \log p(i,j) \tag{13}$$

where $p(i,j)$ is the probability of occurrence of intensity in position (i,j).

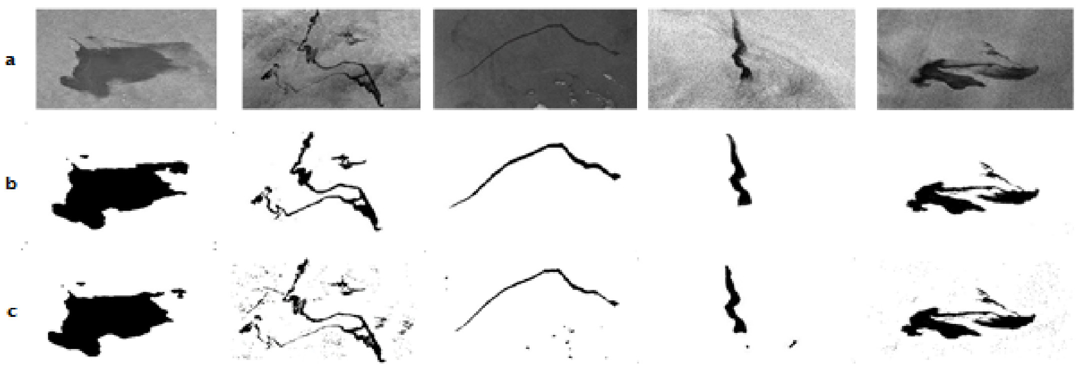

Figure 4. (a) Input image, (b) Image mask (c) Image thresholded by the proposed method.

Correlation: The correlation index (ρ) is the degree of dependence of the gray level of a pixel on the values of its neighbors in the whole image. The Correlation feature of an image is defined (13) as follows:

$$\rho = \sum_i \sum_j \frac{(i-\mu_X)(j-\mu_Y)}{\sigma_X \sigma_Y} p(i,j) \tag{14}$$

Sum of squares variance: Variance is a measure of the dispersion of a set of pixels. The variance shows the dispersion of the gray levels of the image relative to the mean. The sum of squares variance of an image is defined (14) as follows:

$$\text{Variance} = \sum_i \sum_j (z_{(i,j)} - \overline{z_{(i,j)}})^2 p(z_{(i,j)}) \tag{15}$$

Homogeneity: Homogeneity in the image indicates the level of uniformity of the gray levels in the neighborhood of the desired pixel. The homogeneity of an image is defined (15) as follows:

$$\text{Homogeneity} = \sum_i \sum_j \frac{p(i,j)}{1+(i-j)^2} \tag{16}$$

Contrast: Contrast is a measurement of the intensity of one pixel and its neighbor on the image. It also determines the amount of local changes in the image, a high contrast photo shows a wide range of dark and light pixels. The texture is more visible in these images. In binary images, high contrast makes the lines bold and reduces details. The contrast of an image is defined (16) as follows:

$$\text{Contras} = \sum_i \sum_j (i-j)^2 p(i,j) \tag{17}$$

5. Results and experiments on real dataset

As mentioned before, in this study, about 206 oil spills and 94 look-alikes images (256×256 pixels) were considered to evaluate the proposed method with the different conditions of resolution, homogeneity, and boundaries quality as shown in Table 2. These datasets contained several images taken by the Envisat, ERS-1/2, RADARSAT-1, TerraSAR-X, Sentinel-1. Some phenomena such as oily ice or convective cells and biological stains create dark spots like oil stains in radar images where it is crucial to choose features that separate oil stains from non-oil stains. Sine these phenomena have different textural and geometrical features.
The evaluation images include 206 images of oil slicks and sea surface and 94 images of similar phenomena and sea surface, where the sea surface and similar phenomena are placed in the non-oil class. Fig. 5 shows the result of the classification of two oil and non-oil classes resulting from the proposed thresholding of the two methods of Otsu and Bradley and the use of selected features.
This evaluation was done using KNN classification and 80% of the data was for training and 20% for testing. According to the obtained results, different classifications have been able to separate two classes of oil and non-oil stains with high accuracy, which indicates that the proposed method has been able to extract dark areas from radar images well, which increases Accuracy is graded. The method proposed in this article was able to achieve an accuracy of 94.9% with one misidentifications of oil slicks and five misidentifications of non-oil slicks.
Furthermore, that the proposed method does not depend on a specific classification, we repeated the simulation using different classifications and the results can be seen in Table 3.
Similar phenomena that are included in the non-oil category have different geometric and textural characteristics, which reduces the accuracy obtained. To improve the identification of oil stains, the selected features can be limited and considered two by two, in addition to reducing the processing time and extraction of oil stains, it improves the classification performance. Table 4 shows the results of this evaluation. According to the results, the use of two features, area and entropy, improves the precision to 96.36%, as demonstrated in Fig. 6.

Table 2. Types of satellites used in the dataset.

Satellite		Polarization	Band
Envisat	ASAR	W	C
ERS-1/2	SAR	W	C
RADARSAT-1	SAR	HH	C
TerraSAR-X	SAR	HH	X
Sentinel-1A	SAR	HH/HV	C
UAVSAR	SAR	Quad-polarization	L

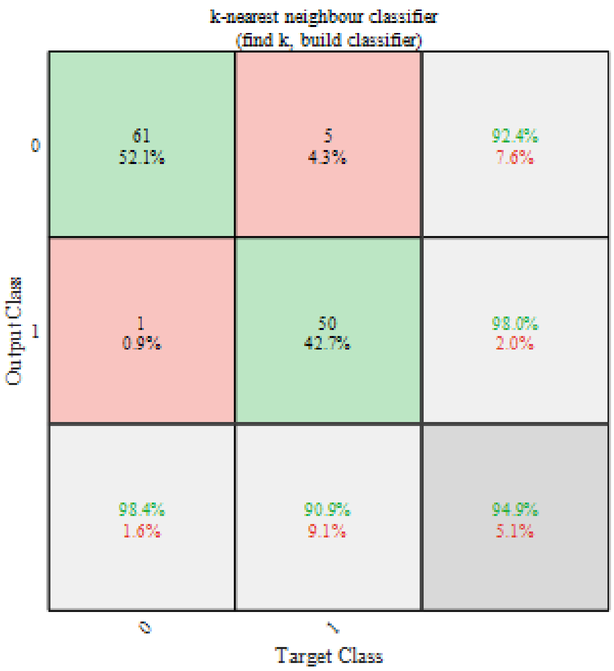

Figure 5. Confusion matrix for KNN classification. 206 oil spills and 94 look-alikes images (256×256 pixels).

Table 3. Comparison of measurement criteria for different classifications.

Classifier	Accuracy	Sensitivity	Precision
Decision tree classifier [20]	94.7	95.2	92.7
Discriminative restricted Boltzmann machine classifier [21]	94.4	97.4	92.3
Linear perceptron [22]	84.6	72.6	91.8
Logistic Regression [23]	93.1	98.2	92.2
Naive Bayes classifier [20]	89.7	90.3	90.3
KNN [20]	**94.9**	**98.4**	**92.4**

Table 4. Comparison of KNN classification precision for pairs of selected features in the proposed method.

Precision	Entropy	VAR	Area	Contrast	Homogeneity	Correlation
Entropy	-	92.4	**96.36**	92.38	91.35	89.67
VAR	92.40	-	96.31	93.21	91.41	90.41
Area	**96.36**	96.31	-	94.89	94.03	91.53
Contrast	92.38	93.20	94.89	-	92.25	90.69
Homogeneity	91.35	91.41	94.03	92.25	-	74.92
Correlation	89.67	90.41	91.53	90.69	74.92	-

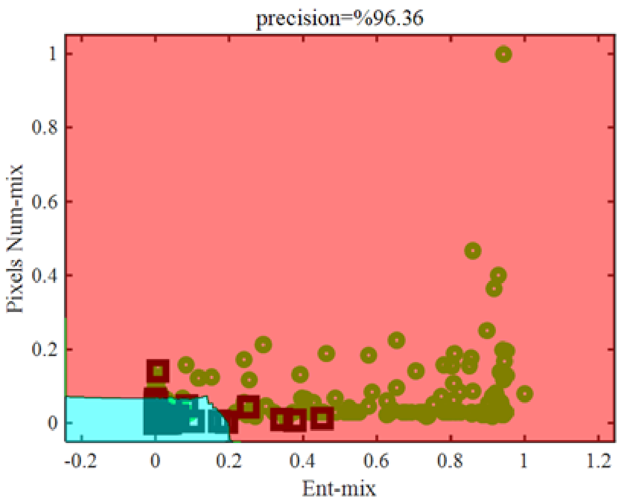

Figure 6. Scatter diagram resulting from the comparison of entropy and area in KNN classification resulting a precision of 96.36%.

6. Conclusion

We proposed a new thresholding method by Using a novel Otsu-Bradley's thresholding method which was able to extract oil slicks with different textures and geometric features from the images with a high PSNR average. Appropriate features were selected that are common in similar phenomena. SAR sensors are commonly utilized in research because of their superior capability in detecting oil pollution when compared to other sensors. Basically, our method detected oil stains and it contained three fundamental stages. The initial process involves removing oil stains or similar occurrences from the images. During the second stage, distinctive characteristics were identified in order to differentiate oil stains from other similar occurrences. In the end, during the third phase, oil stains and similar occurrences were categorized into various groupings. The results of different classifications show that they are able to classify the samples correctly. The success of the proposed Otsu-Bradley's thresholding method can be attributed to the combination of geometric and texture features. By incorporating the shape-based information and the texture-based features, this method achieves the ability to effectively distinguish between oil slicks and other water surface features. This claim has been investigated by separating two by two features extracted in this research in the form of a scatter diagram. According to the results, the method was able to achieve an accuracy of 94.9% with one misidentifications of oil slicks and five misidentifications of non-oil slicks. We repeated the classification using two features, entropy and area, which improved the precision to 96.36%.

Authors contributions
Authors have contributed equally in preparing and writing the manuscript.

Availability of data and materials
The data that support the findings of this study are available from the corresponding author upon reasonable request.

Conflict of interests
The authors declare that they have no known competing financial interests or personal relationships that could have appeared to influence the work reported in this paper.

References

[1] A. Niyazi, M. Majidi Nezhad, A. Heydari, D. Astiaso Garcia, and G. Sylaios. "**A principal component analysis methodology of oil spill detection and monitoring using satellite remote sensing sensors**.". 15(5):1460, 2023.
DOI: https://doi.org/10.3390/rs15051460.

[2] Z. Qiqi et al. "**Oil spill contextual and boundary-supervised detection network based on marine SAR images**.". *IEEE Transactions on Geoscience and Remote Sensing*, 60, 2021.
DOI: https://doi.org/10.1109/TGRS.2021.3115492.

[3] S. Alaa, M. Alkasassbeh, M. Braik, and H. Abu Ayyash. "**Detection of oil spills in SAR images using threshold segmentation algorithms**.". *Malaysia: Green Building Index*, 57(7), 2012.
DOI: https://doi.org/10.5120/9125-3291.

[4] N. Aghaei, G. Akbarizadeh, and A. Kosarian. "**GreyWolfLSM: An accurate oil spill detection method based on level set method from synthetic aperture radar imagery**.". *Eur. J. Remote Sens.*, pages 1–8, 2022.
DOI: https://doi.org/10.1080/22797254.2022.2037468.

[5] L. W. Mdakane and W. Kleynhans. "**Feature selection and classification of oil spill from vessels using Sentinel-1 wide–swath synthetic aperture radar data**.". *IEEE Geoscience and Remote Sensing Letters*, 19(5):1–5, 2020.
DOI: https://doi.org/10.1109/LGRS.2020.3025641.

[6] M. Marghany. "**Oil spill pollution automatic detection from MultiSAR satellite data using genetic algorithm**.". *Adv. Geosci. Remote Sensing*, page 51–71, 2014.
DOI: https://doi.org/10.5772/58572.

[7] D. Moroni, G. Pieri, and M. Tampucci. "**Environmental decision support systems for monitoring small scale oil spills: Existing solutions, best practices and current challenges**.". *Journal of Marine Science and Engineering*, 7(1):19, 2019.
DOI: https://doi.org/10.3390/jmse7010019.

[8] Q. Zhu, Y. Zhang, Z. Li, X. Yan, Q. Guan, Y. Zhong, L. Zhang, and D. Li. "**Oil spill contextual and boundary-supervised detection network based on marine SAR images**.". *IEEE Transactions on Geoscience and Remote Sensing*, 60:1–10, 2021.
DOI: https://doi.org/10.1109/TGRS.2021.3115492.

[9] K. Zeng and Y. Wang. "**A deep convolutional neural network for oil spill detection from spaceborne SAR images**.". *Remote Sensing*, 12(6):1015, 2020.
DOI: https://doi.org/10.3390/rs12061015.

[10] M. Nieto-Hidalgo, A. J. Gallego, P. Gil, and A. Pertusa. "**Two-stage convolutional neural network for ship and spill detection using SLAR images**.". *IEEE Transactions on Geoscience and Remote Sensing*, 56(9):5217–5230, 2018.
DOI: https://doi.org/10.1109/TGRS.2018.2812619.

[11] D. Cantorna, C. Dafonte, A. Iglesias, and B. Arcay. "**Oil spill segmentation in SAR images using convolutional neural networks. A comparative analysis with clustering and logistic regression algorithms**.". *Applied Soft Computing*, 84:105716, 2019.
DOI: https://doi.org/10.1016/j.asoc.2019.105716.

[12] M. Shaban, R. Salim, H. Abu Khalifeh, A. Khelifi, A. Shalaby, S. El-Mashad, A. Mahmoud, M. Ghazal, and A. El-Baz. "**A deep-learning framework for the detection of oil spills from SAR data**.". *Sensors*, 21(7):2351, 2021.
DOI: https://doi.org/10.3390/s21072351.

[13] D. Song, Z. Zhen, B. Wang, X. Li, L. Gao, N. Wang, T. Xie, and T. Zhang. "**A novel marine oil spillage identification scheme based on convolution neural network feature extraction from fully polarimetric SAR imagery**.". *IEEE Access*, 8:59801–59820, 2020.
DOI: https://doi.org/10.1109/ACCESS.2020.2979219.

[14] D. Mera, V. Bolon-Canedo, J. M. Cotos, and A. Alonso-Betanzos. "**On the use of feature selection to improve the detection of sea oil spills in SAR images**.". *Comput. Geosci.*, 100:166–178, 2017.
DOI: https://doi.org/10.1016/j.cageo.2016.12.013.

[15] C. Huang, X. Li, and Y. Wen. "**An Otsu image segmentation based on fruitfly optimization algorithm**.". *Alexandria Eng. J.*, 60(1): 183–188, 2020.
DOI: https://doi.org/10.1016/j.aej.2020.06.054.

[16] A. Abdusalomov, M. Mukhiddinov, O. Djuraev, U. Khamdamov, and T. K. Whangbo. "**Automatic salient object extraction based on locally adaptive thresholding to generate tactile graphics**.". *Applied Sciences*, 10:3350, 2020.
DOI: https://doi.org/10.3390/app10103350.

[17] H. Jafarzadeh, M. Mahdianpari, S. Homayouni, F. Mohammadimanesh, and M. Dabboor. "**Oil spill detection from synthetic aperture radar earth observations: A meta-analysis and comprehensive review**.". *Giscience Remote Sens.*, 58(7):1022–1051, 2021.
DOI: https://doi.org/10.1080/15481603.2021.1952542.

[18] U. Sara, M. Akter, and M. S. Uddin. "**Image quality assessment through FSIM, SSIM, MSE and PSNR—A comparative study**.". *J. Comput. Commun.*, 7(3):8–18, 2019.
DOI: https://doi.org/10.4236/jcc.2019.73002.

[19] P. K. Mall, P. K. Singh, and D. Yadav. "**GLCM based feature extraction and medical X-ray image classification using machine learning techniques**.". *IEEE Conf. Inf. Commun. Technol.*, pages 1–6, 2019.
DOI: https://doi.org/10.1109/CICT48419.2019.9066263.

[20] P. C. Sen, M. Hajra, and M. Ghosh. "**Supervised classification algorithms in machine learning: A survey and review**.". *Advances in Intelligent Systems and Computing*, pages 99–111, 2019.
DOI: https://doi.org/10.1007/978-981-13.

[21] H. Jafarzadeh, M. Mahdianpari, S. Homayouni, F. Mohammadimanesh, and M. Dabboor. "**Oil spill detection from Synthetic Aperture Radar Earth observations: A meta-analysis and comprehensive review**.". *GIScience & Remote Sensing*, 58(7):1022–1051, 2021.
DOI: https://doi.org/10.1080/15481603.2021.1952542.

[22] V. Kurkova and M. Sanguineti. "**Approximation of classifiers by deep perceptron networks**.". *Neural Net.*, 165:654–661, 2023.
DOI: https://doi.org/10.1016/j.neunet.2023.06.004.

[23] R. MurtiRawat, S. Panchal, V. K. Singh, and Y. Panchal. "**Breast cancer detection using K-nearest neighbors, logistic regression and ensemble learning**.". *Proc. Int. Conf. Electron. Sustain. Commun. Syst.*, page 534–540, 2020.
DOI: https://doi.org/10.1109/ICESC48915.2020.9155783.